Supporting Information

Azimuthal Anisotropy Induced by Partial Flux-closure in Self-assembled Tubular Permalloy Membranes

Balram Singh,[1,2] Valeria M. A. Salinas,[3] Markus Loeffler,[4] Ivan Soldatov,[2] Boris Rivkin,[2] Martin Hantusch,[2] Bernd Rellinghaus,[4] Rudolf Schäfer,[2,5] Jorge A. Otálora,[3] and Volker Neu[2]

[1] *Institute of Applied Physics, TU Wien, 1040 Vienna, Austria*

[2] *Leibniz Institute for Solid State and Materials Research Dresden, Helmholtzstr. 20, D-01069 Dresden, Germany*

[3] *Departamento de Física, Universidad Católica del Norte, Avenida Angamos 0610, Casilla 1280, Antofagasta, Chile*

[4] *Dresden Centre for Nanoanalysis, TU Dresden, 01069 Dresden, Germany*

[5] *Institute for Materials Science, TU Dresden, 01062 Dresden, Germany*

(Dated: April 24, 2025)

1 Stress-induced magnetic anisotropy of thin-film

We examined the film's anisotropic behavior under mechanical stress to investigate the magnetostriction of NiFe films deposited on glass substrates used in rolling experiments. The stress was applied by bending the film substrate using the setup illustrated in Figure S1. The sample was positioned to induce tensile stress in the magnetic film, so the Py film was on the convex (top) surface. Conversely, to apply compressive stress, the sample was oriented so that the Py film was on the concave (bottom) surface, with observations made through the transparent substrate.

The in-plane angular distribution of coercivity and the M_r/M_s ratio were determined from angle-resolved Kerr measurements, from 0° to 180° in 3° increments, as described in [1] for both unstressed and stressed states. As shown in Figure S1 (b-i, b-ii, c-i, c-ii), both samples exhibit uniaxial anisotropy, which does not change under tensile or compressive stress. Despite minor variations in the coercive field values, the orientation of the uniaxial easy axis remains unchanged. This behavior contrasts with similar but non-zero magnetostrictive NiFe films, which alter their anisotropy axis when subjected to mechanical stress. [1]

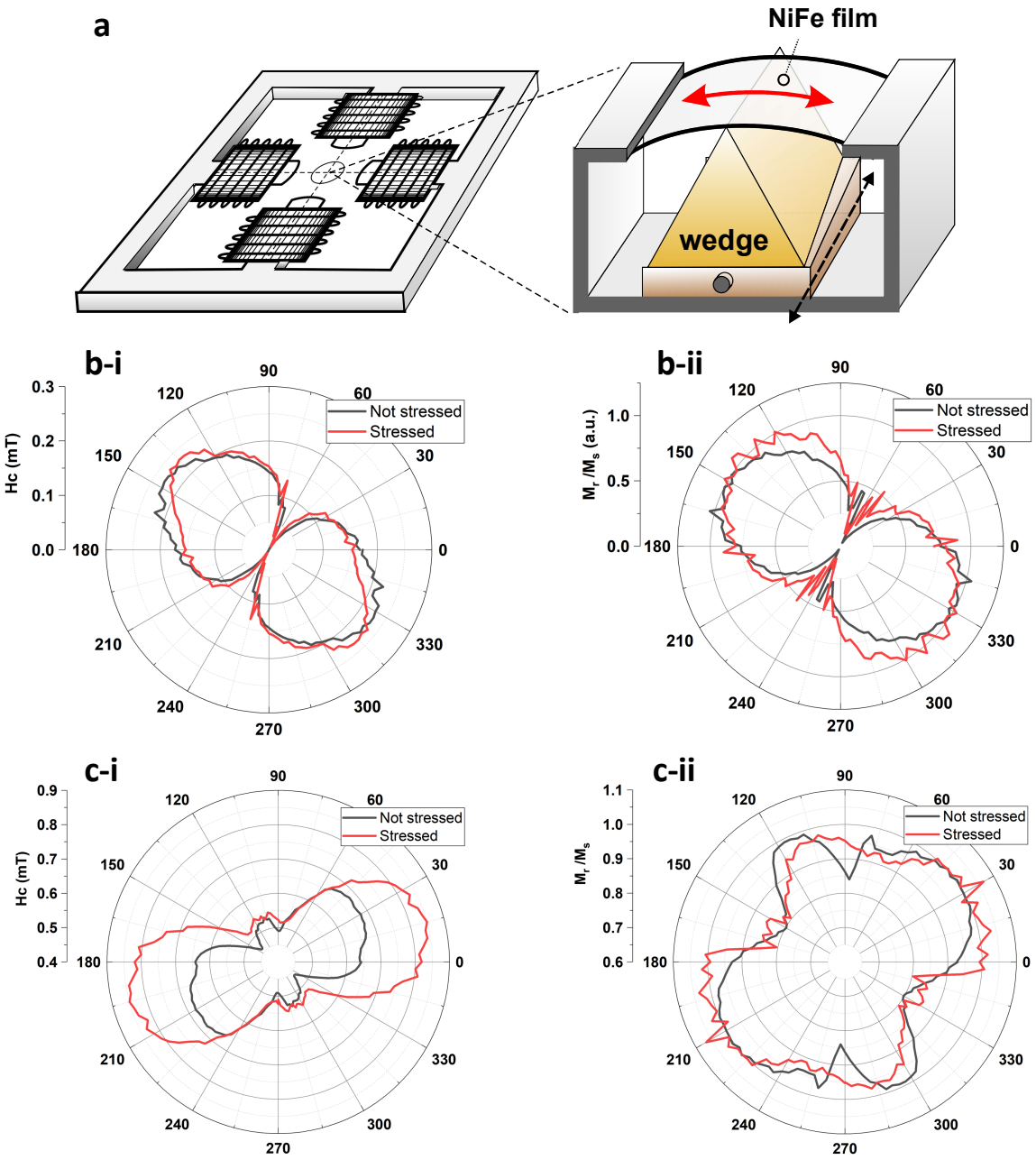

FIG. S1: Schematics of the experiment and anisotropy of NiFe samples. (a) Quadrupole magnets can generate fields in arbitrary directions in the xy-sample plane and sample holder for stress application. (b-i) and (b-ii) Angular dependencies of coercive field and remanent magnetization of the sample prepared with the film deposited on the polymeric platform for rolling up in the as-prepared state and under applied tensile stress, respectively. (c-i) and (c-ii) Angular dependencies of coercive field and remanent magnetization of the sample prepared with the film deposited on the polymeric platform for rolling-down, in the as-prepared state and under applied compressive stress, respectively.

To determine the uniaxial anisotropy constant, the magnetization reversal curve was measured along the hard axis (at angle 111° in Figure S1 (c-i, c-ii) in an anhysteretic mode. In this mode, each field measurement point is obtained under a DC magnetic field, superimposed with a decaying alternating magnetic field, ensuring the system reaches a local equilibrium state. This method yields hysteresis-free magnetization curves, allowing for the direct determination of the anisotropy field H_a. The anisotropy field H_a is identified at the point where a linear fit of the measurement data in the linear region approaches saturation (illustrated by the red curve in Figure S2). Using the measured anisotropy field value $H_a = 0.22\,\mathrm{mT}$ and the saturation polarization $M_s = 690\,\mathrm{kA/m}$ for NiFe, the uniaxial anisotropy constant

$K_{growthinducedanisotropy}$ is calculated as:

$$K_{growthinducedanisotropy} = \frac{1}{2}\frac{M_s H_a}{4\pi\mu_0}$$

This yields $K_{growthinducedanisotropy} = 70\,\mathrm{J/m^3}$, indicating that the grown film has relatively low anisotropy.

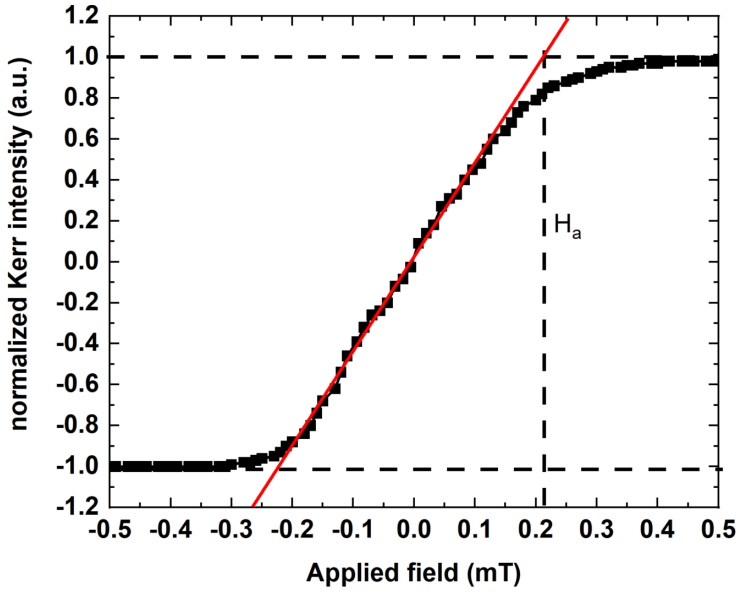

FIG. S2: Anhysteretic magnetization curves of NiFe film (prepared together with the film deposited on the polymeric platform for rolling-down) as measured by Kerr magnetometry along the in-plane hard axis (at angle 111°).

2 X-ray computed tomography (XCT) imaging of 3D tubular architectures

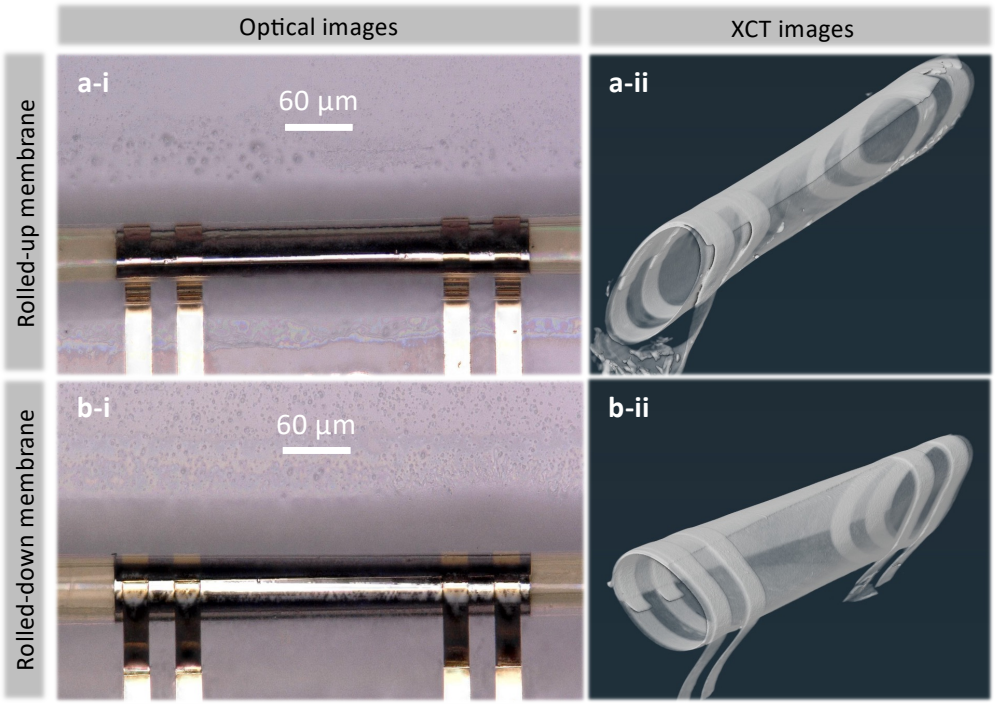

FIG. S3: Top-view (optical) and 3-dimensional (XCT) images of rolled-up (a-i and a-ii) and rolled-down (b-i and b-ii) membranes.

3 AMR curves for all the rolled membranes

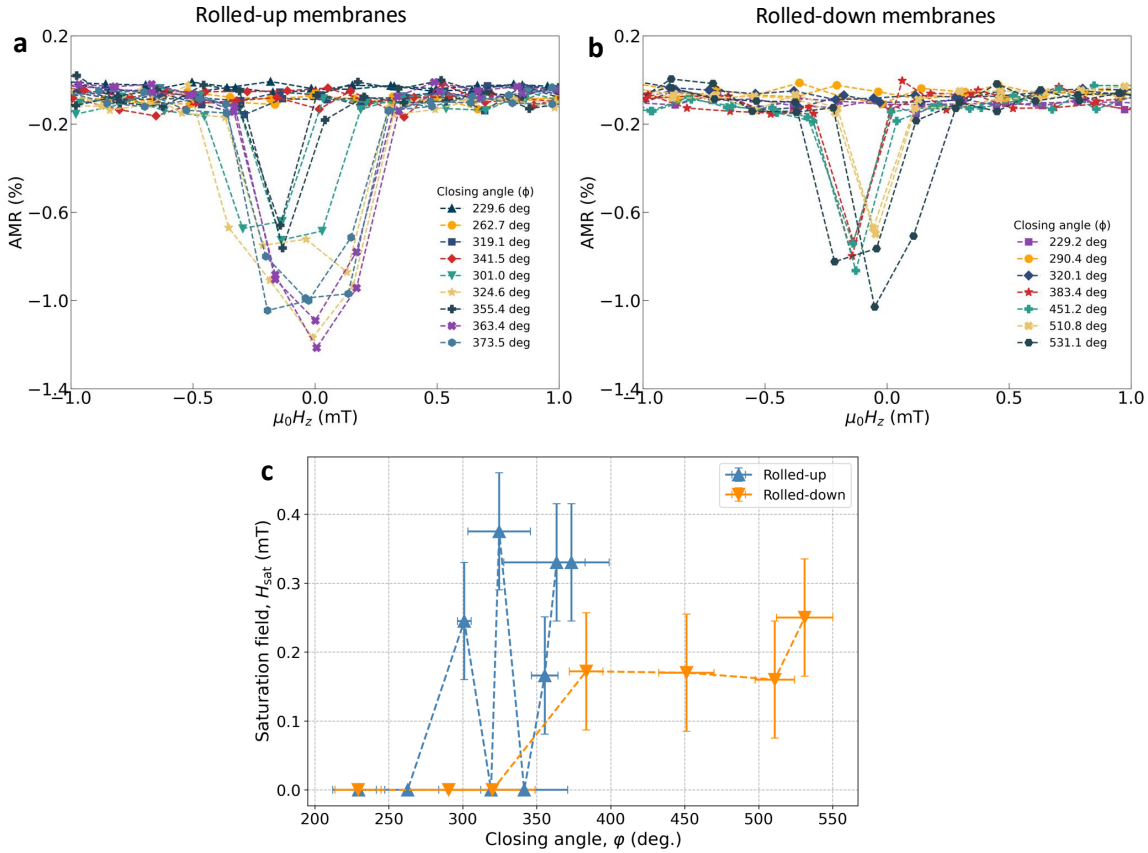

FIG. S4: AMR curves for the (a) rolled-up and (b) rolled-down membranes of different closing angles, φ (c) Saturation fields of the AMR curves as a function of the closing angle.

4 Analytical calculation of magnetostatic anisotropies

To calculate the anisotropy constants of thin films with different degrees of curvature, going from a flat system (see Figure S5a-i) to a curved one until forming a tube (see Figure S5b-i) requires rewriting the magnetostatic energy (also known as dipolar energy or self-energy) of the system in terms of uniaxial anisotropy. It is accomplished by considering a monodomain system analogous to the Stoner-Wohlfarth model. This leads to an expression of anisotropy as a function of the demagnetizing factors, including all geometrical aspects of the film.

A Dipolar Energy

The dipolar energy is the energy stored in the dipole interactions between the magnetic moments of atoms or magnetic regions within the material. To compute the magnetostatic energy, which depends on the magnetization $\mathbf{M}$ and the corresponding demagnetizing field $\mathbf{H}_d$, the magnetostatic potential Φ must first be calculated as [2]:

$$\Phi(\mathbf{r}) = \frac{1}{4\pi}\int_V \frac{\rho(\mathbf{r}')}{|\mathbf{r}-\mathbf{r}'|}\,d^3r' + \frac{1}{4\pi}\int_S \frac{\sigma(\mathbf{r}')}{|\mathbf{r}-\mathbf{r}'|}\,dS' \tag{1}$$

where $\rho(\mathbf{r}')$ and $\sigma(\mathbf{r}')$ represent the volumetric and surface magnetic charge densities, respectively.

From this, the demagnetizing field $\mathbf{H}_d$ can be obtained as the negative gradient of the potential [2]:

$$\mathbf{H}_d = -\nabla\Phi \tag{2}$$

Once the field is obtained, an integration over the volume of the system allows us to find the self-induced energy as [2]

$$E_d = -\frac{1}{2}\mu_0 \int \mathbf{M}\cdot\mathbf{H}_d\,dV \tag{3}$$

where $\mu_0 = 4\pi\times10^{-7}$ H/m is the vacuum permeability. However, it is also known that in the case of a monodomain, the demagnetizing field $\mathbf{H}_d$ is related to the demagnetizing tensor $\overleftrightarrow{D}$ and the magnetization $\mathbf{M}$ as follows [2]:

$$\mathbf{H}_d = -\overleftrightarrow{D}\cdot\mathbf{M} \tag{4}$$

B Demagnetizing Tensor

Considering that the samples are uniformly magnetized up to saturation, the linear relation in Eq. (4) can be established, where $\overleftrightarrow{D}$ represents a second-order tensor according to Eq. (5).

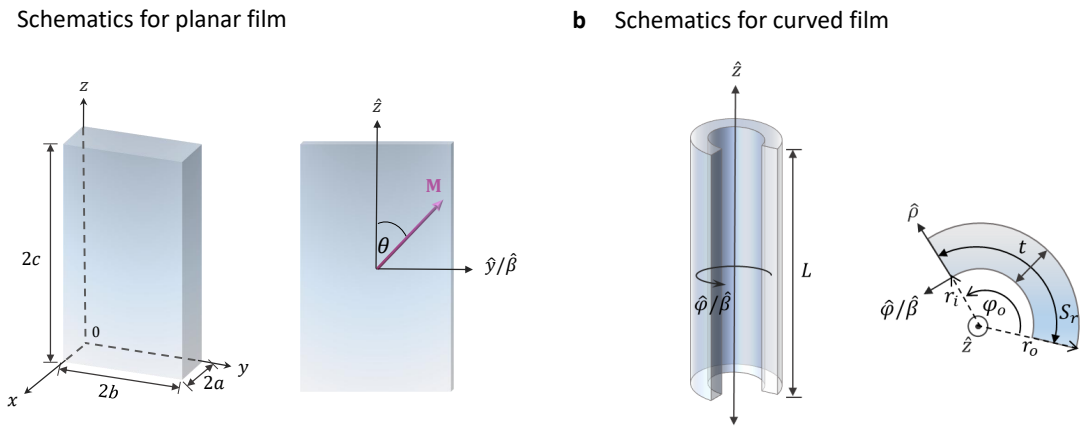

FIG. S5: Schematic for the coordinate system for (a) planar and (b) curved membrane.

$$\overleftrightarrow{D} = \begin{pmatrix} D_{xx} & D_{xy} & D_{xz} \\ D_{yx} & D_{yy} & D_{yz} \\ D_{zx} & D_{zy} & D_{zz} \end{pmatrix}, \tag{5}$$

$$\overleftrightarrow{N} = \frac{1}{V} \int \overleftrightarrow{D}\, d^3r, \tag{6}$$

and $N_{xx} + N_{yy} + N_{zz} = 1$.

A new expression for the dipolar energy in terms of the demagnetizing factors can be derived using Eq. (4) and Eq.(3), such as

$$E_d = \frac{1}{2}\mu_0 V M_s^2 \sum_{i,j} N_{ij} m_i m_j, \tag{7}$$

where M_s is the saturation magnetization, and m represents the components of the magnetization along different directions, respectively, with $i = x, y, z$ and $j = x, y, z$.

C Anisotropy Energy

Due to the system's geometry, it will exhibit some preferred directions of magnetization that require less energy. This phenomenon is known as shape anisotropy, and it's the type of anisotropy considered in this work. By solving Eq. (3), the demagnetizing factors are determined using Eq. (8), allowing the dipolar energy to be rewritten as a uniaxial anisotropy energy [5].

$$E_{\text{ani}} = K_u \sin^2(\theta) \tag{8}$$

This way, it is possible to obtain the appropriate anisotropy constant K_u, which can be expressed in terms of the demagnetizing factors N_{ij}, where θ is the angle formed by the magnetization with the z-axis in the ZY plane. Higher-order contributions to the anisotropy energy are ignored.

While the method may seem straightforward, the algebra involved is not that trivial. Some details on the resolution of the integrals for Eq.(3), the energy rescaling when writing Ed as Eq.(8), and its comparison with the SW-model are mentioned in the following subsections.

D Coordinate systems and reference frames

For the thin membranes, the approximation of a rectangular prism was considered. The origin of this prism was set at one of its lower corners, with dimensions $0 < x \leq 2a$, $0 < y \leq 2b$, and $0 < z \leq 2c$, as shown in Figure S5a.

The curvature suggests a more suitable coordinate system for the curved geometry: cylindrical coordinates, where $z \to z$, $y \to \varphi$, and $x \to \rho$. In this case, the reference frame is shown in Figure S5b.

Consequently, a parameter β is introduced to simplify notation and facilitate the analysis, which refers to the y and φ_0 directions in the planar and curved cases, respectively. Therefore, if the magnetization forms an angle θ with respect to the z-axis, its components can be written as $\mathbf{M} = M_s \sin(\theta)\,\hat{\beta} + M_s \cos(\theta)\,\hat{z}$.

E Demagnetizing factors

A homogeneous magnetization along the z-axis is considered for the planar case. This makes the first (volume) term in Eq.(1) vanish, and only the second (surface) term is considered in the following. Due to the system's symmetry, if the result of a single demagnetizing factor—N_{zz} in this case—is known, the other demagnetizing factors can be determined using the following relations:

- $N_{xx}(a,b,c) = N_{zz}(c,b,a)$
- $N_{yy}(a,b,c) = N_{zz}(a,c,b)$

and, using the previously described method, it is possible to calculate this factor as was derived initially by Aharoni [3].

In the curved case, if the magnetization is decomposed into its two components as $\mathbf{M} = M_s \sin(\theta)\,\hat{\varphi} + M_s \cos(\theta)\,\hat{z}$, the magnetostatic potential of Eq. 1 is also decomposed into azimuthal $\hat{\varphi}$ and $\hat{z}$ contributions. This results in a magnetostatic energy of the following form:

$$E_d = -\frac{1}{2}\mu_0 M_s \int \left(H_\varphi \sin(\theta) + H_z \cos(\theta)\right)\, dV \tag{9}$$

From here, we can deduce the demagnetizing factors N_{zz} and $N_{\varphi\varphi}$ by assuming the magnetization aligned along $\hat{z}$ ($\theta = 0$) or $\hat{\varphi}$ ($\theta = \pi/2$) axis, respectively, and manipulating Eq. 9, as shown in the following for N_{zz} ($\theta = 0$):

Considering the specific case of $\mathbf{M} = M_z = M_s$, the magnetostatic energy (Eq. 9) and the demagnetizing field (Eq. (4)) reduce to

$$E_d = -\frac{1}{2}\mu_0 M_s \int H_z\, dV, \tag{10}$$

and

$$\mathbf{H}_d = H_z = -\nabla\Phi = -\frac{M_s}{4\pi}\int_0^{\varphi_0} d\varphi' \int_{r_i}^{r_o} \rho'\, d\rho'\, \partial_z \left(\frac{1}{|\mathbf{r}-\mathbf{r}'|_{z'=L}} - \frac{1}{|\mathbf{r}-\mathbf{r}'|_{z'=0}}\right), \tag{11}$$

where $|\mathbf{r}-\mathbf{r}'| = \sqrt{\rho^2 + \rho'^2 + (z-z')^2 - 2\rho\rho'\cos(\varphi-\varphi')}$.

By substituting the field $\mathbf{H}_d$ from Eq. (11) into Eq. (10), we obtain the following expression for the dipolar energy

$$E_d = \frac{1}{8\pi}\mu_0 M_s^2 \int_0^{\varphi_0} d\varphi \int_{r_i}^{r_o} \rho\, d\rho \left[\int_{r_i}^{r_o} \rho'\, d\rho' \int_0^{\varphi_0} d\varphi' \left(\frac{1}{|\mathbf{r}-\mathbf{r}'|_{z'=L}} - \frac{1}{|\mathbf{r}-\mathbf{r}'|_{z'=0}}\right)_{z=0}^{z=L}\right]. \tag{12}$$

On the other hand, Eq. (7) reduces to

$$E_d = \frac{1}{2} V \mu_0 M_s^2 N_{zz}, \tag{13}$$

and thus, the factor N_{zz} can be obtained as

$$N_{zz} = \frac{2E_d}{V \mu_0 M_s^2}, \tag{14}$$

where E_d is calculated from Eq. (12). Knowing that the volume is $V = \varphi_0 \cdot L \cdot \left(\frac{b^2-a^2}{2}\right)$, we can deduce the demagnetizing factors as

$$N_{zz} = \frac{1}{\pi \varphi_0 (r_o^2 - r_i^2) L} \int_{r_i}^{r_o} d\rho \int_0^{\varphi_0} d\varphi \int_{r_i}^{r_o} d\rho' \, \left[F_2(\rho, \rho', \varphi, \varphi_0) - F_1(\rho, \rho', \varphi, \varphi_0, L)\right] \tag{15}$$

where F_1 is a function expressed in terms of first-order incomplete elliptic integrals

$$F_1(\rho, \rho', \varphi, \varphi_0, L) = \frac{\rho \rho'}{\sqrt{L^2 + (\rho - \rho')^2}} \left[F\left(\frac{\varphi}{2}, -A\right) - F\left(\frac{\varphi - \varphi_0}{2}, -A\right)\right], \tag{16}$$

with $A = \dfrac{4\rho\rho'}{L^2 + (\rho - \rho')^2}$. The structure $F[\ ,\ ]$ denotes the incomplete elliptic integral of the first kind. Additionally, $F_2(\rho, \rho', \varphi, \varphi_0)$ is defined as the limit case of F_1 when $L \to 0$, that is $F_2(\rho, \rho', \varphi, \varphi_0) = F_1(\rho, \rho', \varphi, \varphi_0, L \to 0)$.

Analogously, for a magnetization of the form $\mathbf{M} = M_\varphi = M_s$, we would obtain the demagnetizing field as

$$\mathbf{H}_d = H_\varphi = -\nabla \Phi = -\frac{1}{\rho} \frac{M_s}{4\pi} \int_{r_i}^{r_o} \rho' \, d\rho' \int_0^L dz' \, \partial_\varphi \left(\frac{1}{|\mathbf{r} - \mathbf{r}'|_{\varphi' = \varphi_0}} - \frac{1}{|\mathbf{r} - \mathbf{r}'|_{\varphi' = 0}} \right), \tag{17}$$

from which we deduce the dipolar energy as

$$E_d = \frac{1}{8\pi} \mu_0 M_s^2 \int_0^L dz \int_{r_i}^{r_o} d\rho \left[\int_{r_i}^{r_o} d\rho' \int_0^L dz' \left(\frac{1}{|\mathbf{r} - \mathbf{r}'|_{\varphi' = \varphi_0}} - \frac{1}{|\mathbf{r} - \mathbf{r}'|_{\varphi' = 0}} \right)_{\varphi = 0}^{\varphi = \varphi_0} \right], \tag{18}$$

therefore, the azimuthal demagnetizing factor takes the form

$$N_{\varphi\varphi} = \frac{2E_d}{V \mu_0 M_s^2}. \tag{19}$$

Since we know E_d from Eq. (18), thus the demagnetizing factor is

$$N_{\varphi\varphi} = \frac{1}{\pi \varphi_0 (r_o^2 - r_i^2) L} \int_{r_i}^{r_o} d\rho \int_{r_i}^{r_o} d\rho' \, \left[G_2(\rho, \rho', L) - G_1(\rho, \rho', \varphi_0, L)\right]. \tag{20}$$

Here, $G1$ is defined as

$$G_1(\rho,\rho',\varphi_0,L) = 2\sqrt{B} - 2\sqrt{L^2+B} - L\log\left(-L+\sqrt{L^2+B}\right) + \frac{1}{2}L\log\left(B+2L\left(L+\sqrt{L^2+B}\right)\right) \tag{21}$$

where $B = \rho^2 + \rho'^2 - 2\rho\rho'\cos(\varphi_0)$, and $G_2(\rho,\rho',L)$ is defined as the limit case of G_1 when $\varphi_0 \to 0$, that is $G_2(\rho,\rho',L) = G_1(\rho,\rho',\varphi_0 \to 0, L)$.

It should be noted that $N_{\rho\rho}$ can also be obtained, given that the trace of the demagnetizing tensor is equal to unity. Therefore $N_{\rho\rho} = 1 - (N_{zz} + N_{\varphi\varphi})$.

F Anisotropy Constants

The results obtained for the magnetostatic energy according to Eq. (7) are used to find the anisotropy constants.

$$E_d = \frac{1}{2}V\mu_0 M_s^2\left[(N_{\beta\beta} - N_{zz})\sin^2(\theta) + N_{zz} + N_{\beta z}\sin(2\theta)\right] \tag{22}$$

where the factors N_{ii} are already known expressions given by Eq. (15), Eq. (20), and [3]. To rewrite E_d as an anisotropy energy, it is first normalized by $K_s = \mu_0 M_s^2/2$, defining the dimensionless energy $\check{E}_d$. Then, it is rescaled by $E_0 = VN_{zz}$, such that we obtain:

$$\tilde{E}_d = \check{E}_d - E_0 = V\left[(N_{\beta\beta} - N_{zz})\sin^2(\theta) + N_{\beta z}\sin(2\theta)\right] \tag{23}$$

where $N_{\beta z} \ll (N_{yy} - N_{zz})$, which allows it to be neglected. Thus, by analogy with the anisotropy energy E_{ani} in Eq.(8), this leads to:

$$K_u = K_s(N_{\beta\beta} - N_{zz}) \tag{24}$$

G Comparison of 'N_{ii}' and 'K_u' for flat and curved membranes

The calculation of 'N_{ii}' and 'K_u' has been carried out for a membrane of thickness 10 nm and 100 nm and lengths L of 480μm with different bending radius between 25μm and 75μm as a function of the closing angle φ and its corresponding equivalence in arc length S (Figure S6). Arc length is calculated using a mean radius approximation as $R = (r_o + r_i)/2$ so $S = 2\ \pi\ R\ \varphi^\circ/360^\circ$. Additionally, the following conversion between the dimensions was used: $2a = (r_o - r_i)$, $2b = S$ and $2c = L$.

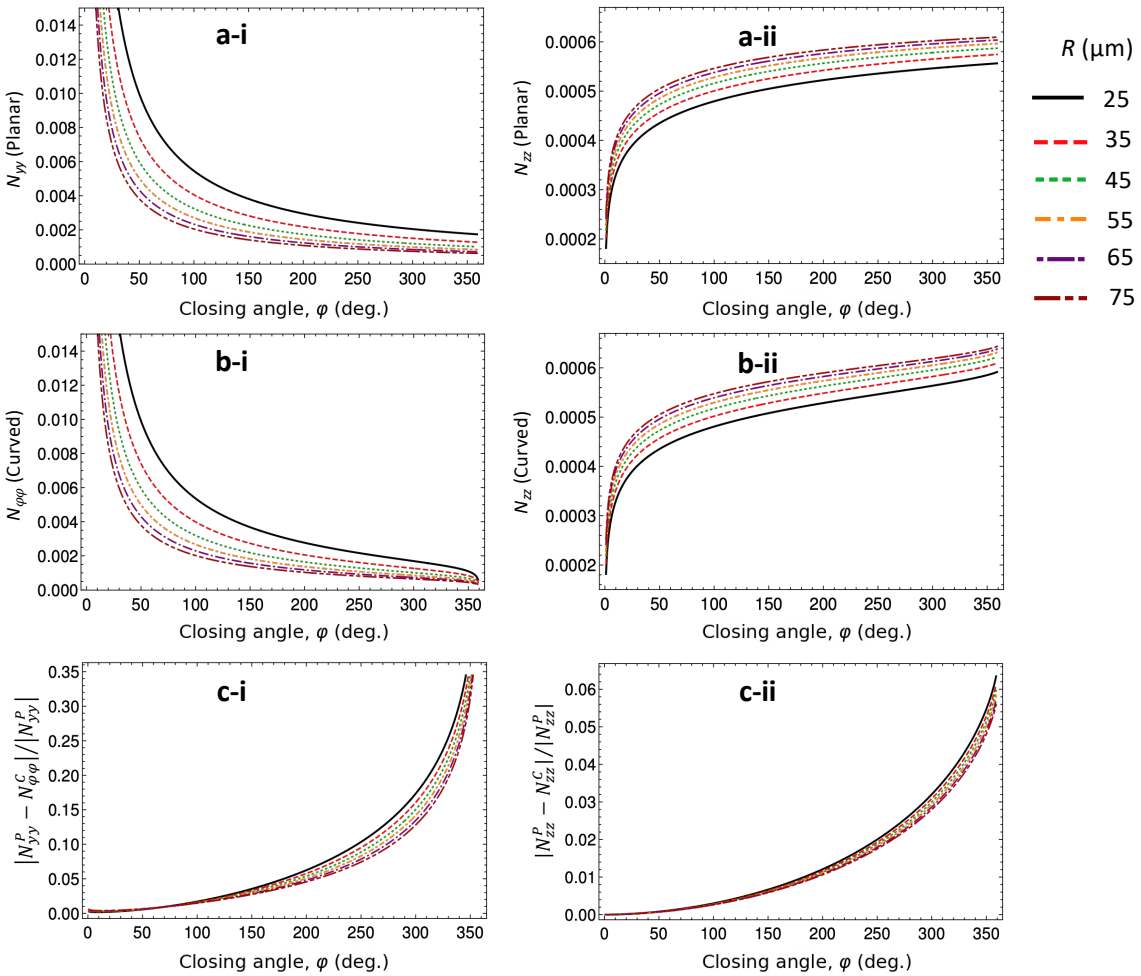

FIG. S6: Demagnetizing factors along two orthogonal directions y- and z-axis of the (a) planar and the (b) curved membranes of length, $L = 480\mu$m, thickness, t=100 nm and different curvature radii as a function of the closing angle φ with its corresponding equivalence in arc length $S[\mu\text{m}]$ for the curved and $2b[\mu\text{m}]$ width for the planar membranes. (c) Normalized difference of demagnetizing factors of planar and curved membranes.

It is understood that the N_{ii} factors depend on the dimensions and tend to increase as these parameters favor a larger cross-sectional area for each factor. Specifically, for N_{zz}, this corresponds to greater thickness and width, while for the $N_{\beta\beta}$ factors, it corresponds to greater thickness and length. The reason is that as these surfaces become larger and closer, the surface charge density and the magnetostatic effect between them increase. All these contributions result in a larger demagnetizing field within the body, and consequently, the magnetization in the respective direction decreases. [4]

With increasing φ, the corresponding $N_{\varphi\varphi}$ decreases, but the 'orthogonal' N_{zz} increases. Similarly, with increasing L, the corresponding N_{zz} decreases, and the orthogonal $N_{\varphi\varphi}$ increases. This behavior is consistent with the results obtained in Figure S6, where it can be noted that both the planar and the curved membranes exhibit quite similar behavior until reaching the point of large closing angles, with the difference becoming more evident for the range in which $\varphi \geq 270°$. In general, it is found that $N_{zzC} > N_{zzP}$ and $N_{\varphi\varphi} < N_{yy}$ when comparing the same equivalent dimensions for each system. The latter, in relation to Eq. (16), results in $k_{1curved} > k_{1planar}$ for the shape anisotropy, accentuating this difference as $\varphi \to 360°$. Another significant difference is shown in Figure S6a-i and Figure S6b-i, where the $N_{\beta\beta}$ factors for the curved system show a drastic drop, with $N_{\varphi\varphi} \to 0$ more easily than its analogue N_{yy}. This can be explained by the magnetostatic interaction of the membrane side edges as they get closer to the closing angle. This also explains why, when $\varphi = 2\pi$ is considered, $N_{\varphi\varphi} = 0$, which implies $H_{d\varphi} = 0$.

Regarding K_u, it is known that, according to the uniaxial anisotropy model, the sign of this constant will determine the energy equilibrium positions to define the orientation of the magnetization. For this reason, the differences between the values of the demagnetizing factors obtained between the planar and the curved membranes are key to

understanding, according to Eq.(16), the different results obtained for the shape anisotropy. In general, we have

$$K_u = \begin{cases} (N_{\beta\beta} - N_{zz}) > 0 & \text{if } L \gg \beta \Rightarrow \theta_{eq} = 0, \pi \\ (N_{\beta\beta} - N_{zz}) < 0 & \text{if } L \ll \beta \Rightarrow \theta_{eq} = \frac{\pi}{2}, \frac{3\pi}{2} \end{cases} \tag{25}$$

Where θ_{eq} is the equilibrium angle of magnetization with respect to the z-axis.[5]

H Shape anisotropy phase diagram

Figure S7a shows a plot similar to Figure 5 in the main manuscript. Figure S7b shows the phase diagrams for 100 nm thick membranes (disks) as before. For comparison, data for the 10 nm thick membranes (stars) are plotted using a radius that is 10 times larger than their actual physical radius. Scaling the radius for the 10 nm data is done only for visualization purposes to highlight the concept of scale invariance.
Specifically, you can see a clear overlap between:
The 100 nm thick membrane with length $L = 4.8\,\mu$m (orange disks), and the 10 nm thick membrane with length $L = 0.48\,\mu$m, plotted with the enlarged radius (green star).
This overlap demonstrates that when the thickness, length, and radius (proportional to the width) of a membrane are all scaled down by the same factor (in this case, 10×), the threshold closing angle of the phase diagram remains unchanged. This behavior reflects a well-known property of demagnetizing factors: scaling down all dimensions of a prism by the same factor does not change its demagnetizing characteristics. Therefore, the observed overlap in Figure S7b provides clear evidence of the scale-invariant nature of the phase diagram.

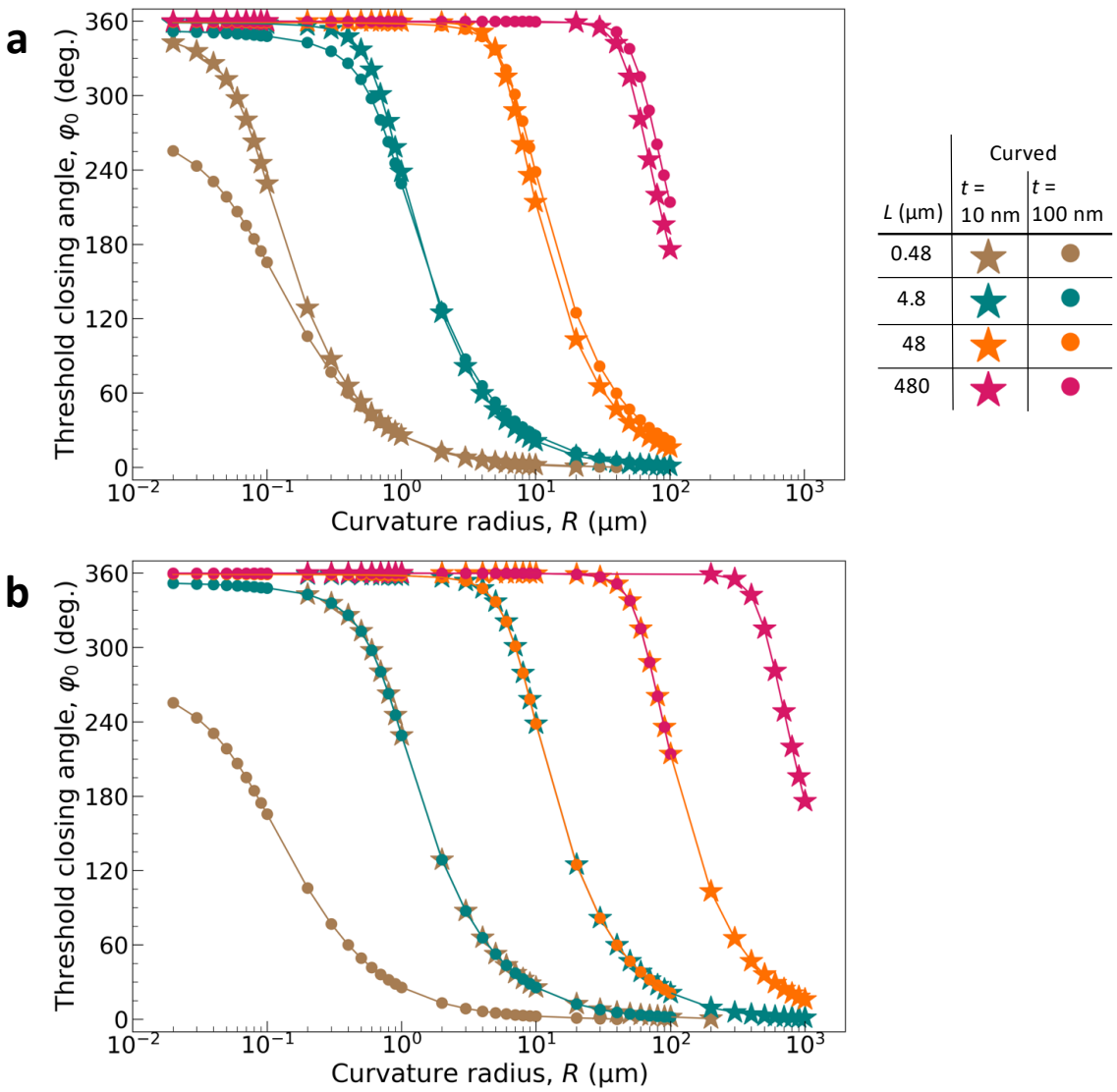

FIG. S7: Shape anisotropy phase diagrams (threshold angles φ_0 vs. R) for curved membranes of different lengths and thicknesses.

I Dependence of the threshold Angle on the groove thickness

An important detail to notice in N_{zz} and $N_{\beta\beta}$ in supporting information Figure S6(a,b) is their dependence on the radius r. Increasing the radius r while φ_0 is maintained constant is equivalent to increasing the arc length in the groove and the width in the prism. Under this transformation, notice that N_{zz} is less susceptible to change than $N_{\beta\beta}$ as the radius increases. As shown, $N_{zz}(N_{\beta\beta})$ shift to higher(lower) values at the order of $10^{-4}(10^{-3})$, when the radius runs from 25 nm to 75 nm. It is an indication of that under this transformation, the demagnetizing field created by the edge surface charges perpendicular to $\hat{\beta}$ is more susceptible to be less antiparallel and weaker than the demagnetizing field created by the surfaces charges perpendicular to $\hat{z}$, as the radius change. This is key to understand the role of the thickness in the demagnetizing factors in the groove, specifically, to understand why the azimuthal flux closure occurs at smaller closing angles for membranes with larger arc length and at larger closing angles for membranes with shorter arc length, when the membrane thickness is reduced from 100 nm to 10 nm. With this end, let´s plot the demagnetizing factors N_{zz} and $N_{\varphi\varphi}$ as function of the closing angle φ_0 at three different thicknesses, 10, 60 and 100 nanometers of a membrane having length $L = 4.8$ μm, and at two different radii separated by one order of magnitude, $r_1 = 500$ nm and $r_2 = 3$ μm. Figure S8 shows the demagnetizing factors N_{zz} and $N_{\varphi\varphi}$ for

the mentioned parameters. It can be noticed that for all the considered thicknesses and closing angles, $N_{\varphi\varphi}$ at $r = 3$ μm takes values in an order of magnitude smaller than at $r = 500$ nm, whereas N_{zz} variates in the same order of magnitude at both radii. It is important to be considered, since it explain why the condition $K_u = 0$ (or equivalently, $N_{\varphi\varphi} = N_{zz}$) occurs at different threshold angles, and showing different dependence with the thickness, as shown by the black-dotted curve in Figure S8 (a) and (b). Since $N_{\varphi\varphi}$ is weaker at $r = 3$ μm, thus the condition $K_u = 0$ occurs at smaller angles, showing a tendency to increase the threshold angle as the thickness increases. Figure S8(d) shows this tendency. Nevertheless, the opposite occurs at $r = 500$ nm where $N_{\varphi\varphi}$ is stronger, where the same condition $K_u = 0$ occurs at larger threshold angles, which decreases as the thickness increases, as shown in Figure S8(c).

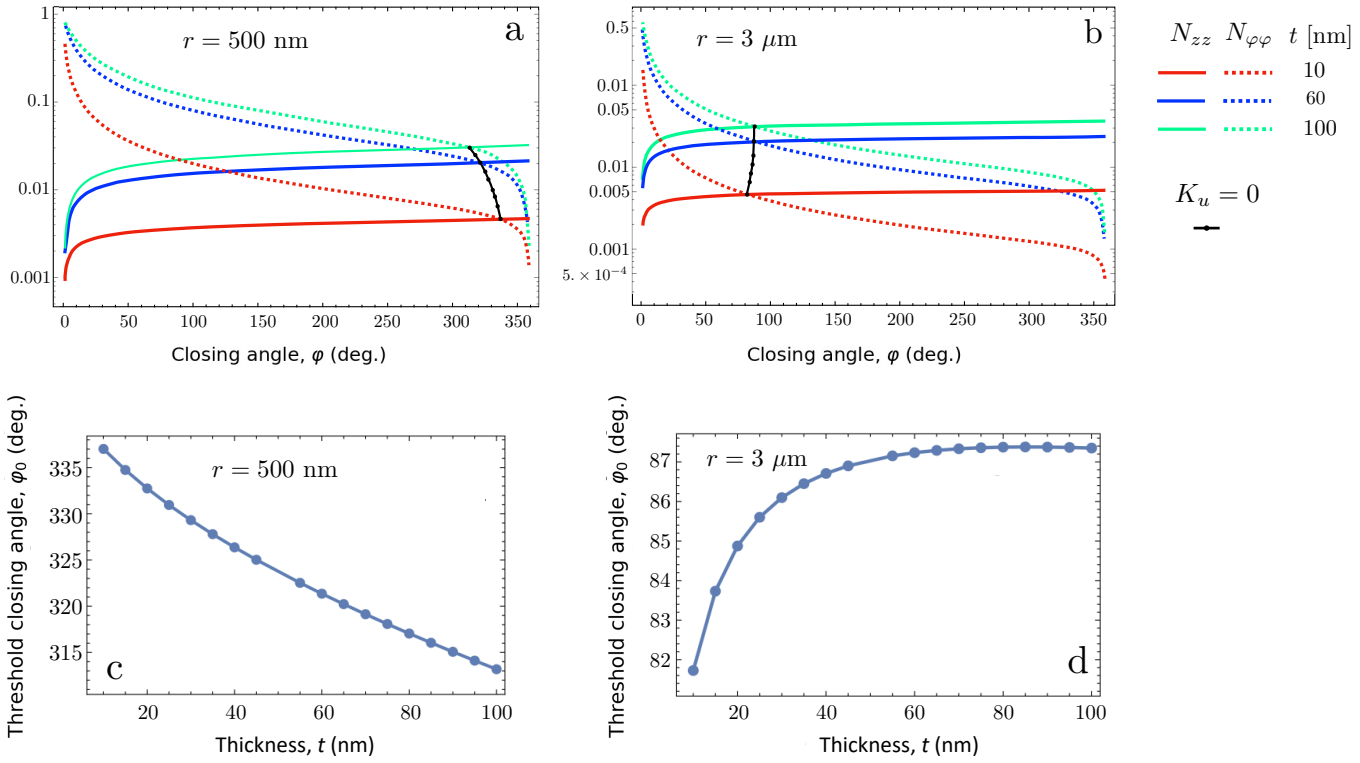

FIG. S8: Demagnetizing factors N_{zz} and $N_{\varphi\varphi}$ for the membranes of length 4.8 μm, at three different thicknesses, 10, 60 and 100 nanometers, and at (a) a radius $r = 500$ nm and (b) $r = 3$ μm. A black dotted curve shows the threshold closing angle at which $K_u = 0$. The threshold angle (φ_0) as a function of the thickness is shown in (c) and (d) for the radii $r = 500$ nm and $r = 3$ μm, respectively.

References

[1] I. V. Saldatov, Journal of Magnetism and Magnetic Materials **529**, 167889 (2021).
[2] A. Aharoni, *Introduction to the Theory of Ferromagnetism* (Clarendon Press, 2000).
[3] A. Aharoni, Journal of Applied Physics **83**, 3432 (1998).
[4] A. Tanakadate, The London, Edinburgh, and Dublin Philosophical Magazine and Journal of Science **26**, 450 (1888).
[5] B. D. Cullity and C. D. Graham, *Introduction to Magnetic Materials* (John Wiley & Sons, 2011).